Review

Fluorescence Microscopy Studies of Porous Silica Materials

Bastian Rühle[†], Melari Davies[†], Thomas Bein, and Christoph Bräuchle

Department of Chemistry and Center for NanoScience (CeNS), University of Munich (LMU), Butenandtstrasse 5 – 13 (E), D-81377 Munich, Germany
[†] These authors contributed equally to the work.

Reprint requests to Prof. Christoph Bräuchle. Fax: +49 (0)89 2180 77548.
E-mail: Christoph.Braeuchle@cup.uni-muenchen.de and Prof. Thomas Bein. Fax: +49 (0)89 2180 77622. tbein@cup.uni-muenchen.de

Z. Naturforsch. **2013**, *68b*, 423 – 444 / DOI: 10.5560/ZNB.2013-3068
Received February 27, 2013

Dedicated to Professor Heinrich Nöth on the occasion of his 85th birthday

In this article, we discuss how fluorescence microscopy techniques are used to investigate important characteristics of porous silica materials. We start with a discussion of the synthesis, formation mechanism and functionalization of these materials. We then give an introduction to single molecule microscopy and show how this technique can be used to gain deeper insights into some defining properties of porous silica, such as pore structure, host-guest interactions and diffusion dynamics. We also provide examples from the literature demonstrating how fluorescence microscopy is used for elucidating important aspects of porous silica materials and heterogeneous catalysis, *e. g.* diffusion properties, reactivity, morphology, intergrowth, accessibility, and catalyst deactivation. Finally, a short outlook on the scope of porous silica hosts in drug delivery applications is given.

Key words: Porous Silica, Fluorescence Microscopy, Single Molecule Spectroscopy, Review Article

Introduction

Porous silica materials are used in a wide variety of applications, including molecular sieves and filters [1, 2], catalysts [3], ion exchangers [4], nanosensors [5], or drug-delivery systems [6, 7]. They are appreciated for their large pore volume, large surface area, and high chemical and structural flexibility and tunability. These properties allow us to tailor the morphology and interaction chemistry of the porous host systems according to the demands of the desired applications. However, in order to be able to efficiently design and synthesize new materials with the envisioned properties, a thorough understanding of the microscopic nature and structure of the host systems and their interactions with guest molecules is of great importance. There are many techniques that can help to gain an overview of the average, bulk properties of these porous systems, such as NMR [8], electron microscopy [9], X-ray diffraction or neutron scattering measurements [10]. However, there are often heterogeneities at a nanoscopic or microscopic level that cannot be assessed with bulk methods, but still play an important role for host-guest interactions and can help us to improve our understanding of the porous host systems. While these heterogeneities can be random, there are also cases in which they reflect intrinsic characteristics of the materials, such as phase separation or domain boundaries. In order to be able to extract such information, single molecule spectroscopy or microscopy measurements are highly desirable.

In this short review article, we briefly describe the synthesis, formation mechanism and functionalization of sol-gel-derived porous silica materials, especially focusing on the evaporation-induced self-assembly (EISA) process for the formation of thin silica films. A brief introduction into single molecule microscopy is given, discussing some technical requirements and important aspects of this technique. We then give an overview of selected cooperative studies performed in our groups at Ludwig-Maximilians-University of Munich, characterizing the details of diffusional dynam-

ics of molecules in different mesoporous materials. These experiments will be introduced by presenting the fundamental study that opened up new ways of understanding the interactions of hosts and guests by combining information from transmission electron microscopy with the diffusion dynamics obtained from single molecule microscopy studies. In addition, we report how synthesis strategies can be optimized by using information gained from single molecule microscopy. We also present a selection of fluorescence microscopy studies from other groups that helped elucidating important aspects of porous silica compounds and heterogeneous catalysis such as diffusion properties, reactivity, morphology, intergrowth, accessibility, and catalyst deactivation. Finally, we give a short outlook on the potential of porous silica hosts in drug delivery applications.

Synthesis of Porous Silica Materials

Micro- and mesoporous silica materials are usually synthesized by a bottom-up approach, in which small organic molecules or surfactants act as a template for the porous structure of the silica framework. Early and prominent examples of this process include the use of alkylammonium ions to control the pore size and periodicity of zeolites, as demonstrated by researchers at the Mobil Oil Corporation in the 1960s [11]. The templating process results in porous, crystalline solids with a well-defined 1-, 2-, or 3-dimensional network of periodically arranged micropores. Later, this approach was further extended to longer-chain alkylammonium ions [12], which yielded a periodic array of mesopores that were approximately 4 nm in diameter or larger, and gave rise to the development of the MCM (Mobil Crystalline Material) family of mesoporous silica materials. The amphiphilic nature (*i. e.* the presence of hydrophilic and hydrophobic parts within one molecule) of the surfactant that acts as the structure-directing agent (SDA) allows for a spontaneous assembly of the latter into micelles, resembling a liquid crystalline phase that gives rise to the periodic porous structure. Meanwhile, a variety of other surfactants have been employed to extend the pore-size and structural diversity even further [13, 14], for example non-ionic triblock-copolymers for the synthesis of the Santa Barbara Amorphous (SBA) type materials [15].

The synthesis strategies mentioned above were originally designed for the synthesis of porous particles that are used in a wide variety of different fields. However, in certain applications such as membranes, low dielectric constant interlayers and sensors, thin films rather than particles are desired. In some of the first approaches that yielded stable, supported mesoporous silica films a substrate was introduced into a silica/surfactant/solvent system in which the initial surfactant concentration was high enough that a micellar phase could be formed (*i. e.* higher than the critical micelle concentration, cmc) [16 – 18]. These approaches allowed for the nucleation of hexagonal silica-surfactant mesophases on the substrate with pores oriented parallel to the substrate surface, and further growth and coalescence over a longer period of time resulted in continuous films. However, these films are often macroscopically inhomogeneous and feature granular textures on micrometer length scales. Another approach that yields very homogeneous films even on macroscopic length scales is the evaporation-induced self-assembly (EISA) approach, introduced by Brinker *et al.* in 1999 [19]. This synthesis strategy employs a homogeneous solution of soluble, inorganic building blocks such as alkoxysilanes (typically tetraethylorthosilicate (TEOS)) and surfactant molecules at concentrations lower than the cmc in a volatile solvent mixture, often comprised of ethanol and water. When coating this solution onto a substrate, preferential evaporation of the volatile solvent leads to an increase in concentration of the surfactant and the non-volatile silica precursor in water. This increase in surfactant concentration in turn leads to a spontaneous self-assembly of silica-surfactant micelles, which further organize into liquid-crystalline mesophases. By altering the molar ratios and chemical nature of the solvent mixture, the silica source, and the surfactant, differently arranged porous mesophases such as 2D-hexagonal, 3D-hexagonal, cubic, and lamellar structures can be obtained [20, 21]. In order for the self assembly process to occur, the silica condensation has to be suppressed or slowed down during the film deposition step by adjusting the pH to a value close to the isoelectric point of colloidal silica (pH $\sim$ 2) [19]. This allows for the cooperative silica-surfactant self-assembly and results in as-deposited films exhibiting liquid-crystalline (*i. e.* semi-solid) behavior. Only after subsequent aging, thermal treatment, or exposure to acid or base catalysis the silica network solidifies in its final pore geometry.

The liquid-crystalline nature of freshly formed films was confirmed by the fact that the tensile stress developed during the mesophase thin film deposition is much lower than that of a similar silica sol prepared without surfactants [19, 22]. Moreover, under certain conditions freshly deposited films could be transformed to a different mesophase (*e. g.* from lamellar to cubic) [20]. Further proof of a structurally flexible material after deposition and deeper insight into the mechanism of mesophase formation and film organization during the EISA process was gained by different groups through *in situ* grazing incidence small-angle X-ray scattering (GISAXS) experiments [22 – 24]. Grosso *et al.* [23] investigated the influence of various experimental parameters on the film formation and organization of films prepared by dip-coating from a silica sol with cetyltrimethylammonium bromide (CTAB) as the SDA. They found that – under otherwise identical conditions – the CTAB-to-TEOS ratio plays the main role in determining the structure of the resulting films. By adjusting this ratio to 0.08, 0.10, or 0.12, 2D-hexagonal, 3D-hexagonal, or cubic phases could be obtained, respectively. They also found that the degree of condensation of the silica species present in the solution (and hence the water content and the aging time of the sol prior to deposition) can have a strong effect on mesophase organization, where the highest degree of organization seems to correlate with a rather high condensation rate. Combining *in situ* XRD measurements with interferometry suggested a formation mechanism that includes the formation of micelles at the film/air interface, a morphological change from elongated to spherical micelles in the case of 3D-hexagonal and 3D-cubic structures, and the existence of a 3D hexagonal intermediate phase prior to the formation of a 3D-cubic structure. In the case of the other structures (*i. e.* 2D-hexagonal and 3D-hexagonal), the authors also observed a transient peak in their XRD patterns. However, unlike in the case of the 3D-cubic structure, they did not attribute this transient peak to a real intermediate structure.

A similar system (namely a silica sol with CTAB as the SDA yielding a 2D-hexagonal mesophase) was also investigated by Doshi *et al.* [22], who carried out time-resolved *in situ* GISAXS studies combined with gravimetric analysis to study the self-assembly of a slowly evaporating film maintained in a horizontal geometry under controlled environmental conditions. This experiment allowed the authors to derive structural and compositional information simultaneously under steady-state conditions. They proposed a mechanism for the formation of the 2D-hexagonal mesophase that included four distinct successive stages during the EISA process, namely an isotropic, a lamellar, a correlated micellar, and finally a 2D-hexagonal geometry, each identified by their respective 2D GISAXS pattern (see Fig. 1).

At the beginning, there are no reflections visible, indicating the lack of any periodic arrangement. Hence, this pattern was assigned to the isotropic phase. In the subsequent phase, a single Bragg reflection can be seen which indicates – in combination with the absence of out-of-plane reflections and combined with the spot orientation and d-spacing – a smectic ordering parallel to the substrate surface. The appearance of such a lamellar phase is unexpected from the bulk phase diagram and the authors attributed it to an interfacial effect. Interestingly, this intermittent lamellar phase could only be observed in the presence of a silica precursor and did not appear under similar conditions when no TEOS was added to the precursor solution. At later stages, the lamellar diffraction spot disappears and a broad, diffuse arc appears concomitantly at larger q-values. This pattern can be explained by the presence of spherical or cylindrical micelles showing a low degree of spatial correlation and hence was assigned to the correlated micellar phase. Over time, the scattering intensified and the width of the arc and its radius decreased. This was attributed to an enhancement of spatial correlation of micelles resulting from their increasing number density and conceivably from their positioning by regular undulations of the lamellar mesophase. Finally, three well-defined Bragg spots defining adjacent 60° central angles with respect to the origin are observed, which can be assigned to a 2D-hexagonal mesophase (*p6mm*) with tube axes oriented parallel to the substrate. Moreover, the authors also observed a disorder-to-order transformation during the EISA process using X-ray reflectivity data and electron microscopy. This transition seems to start at the solid-liquid and at the liquid-air interfaces, and then to propagate to the middle of the film. Similar observations were also made by other groups and for other surfactants, *e. g.* non-ionic triblock-copolymers [20, 23, 25].

Besides the cooperative mechanism discussed above, in which surfactant molecules and inorganic species combine first to form hybrid intermediate species which then further self-assemble into the final

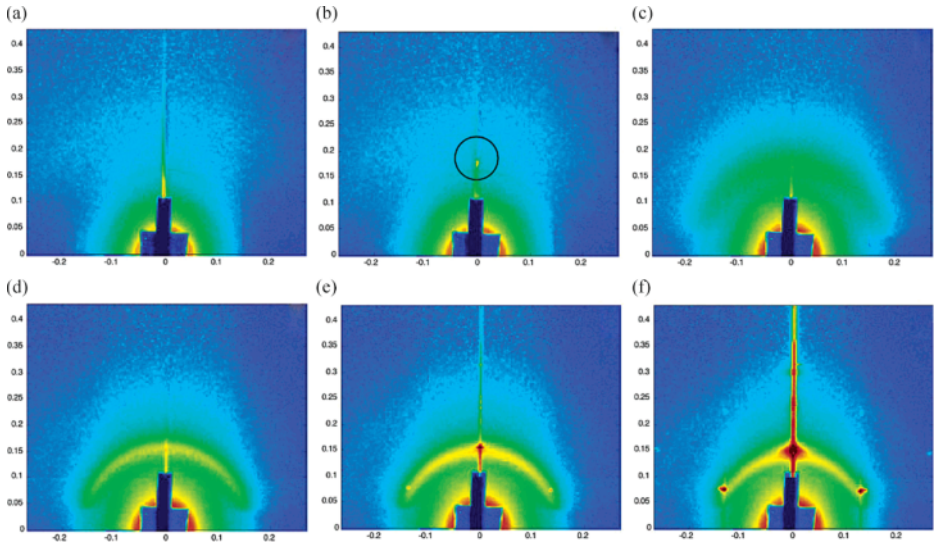

Fig. 1 (color online). GISAXS patterns obtained at different points in time during the formation of a CTAB-templated, 2D-hexagonal thin silica film. The patterns correspond to the following phases: (a) the isotropic phase, (b) the lamellar mesophase, (c and d) the correlated micellar, and (e and f) the hexagonal mesophase. Reprinted with permission from ref. [22]. Copyright 2003 American Chemical Society.

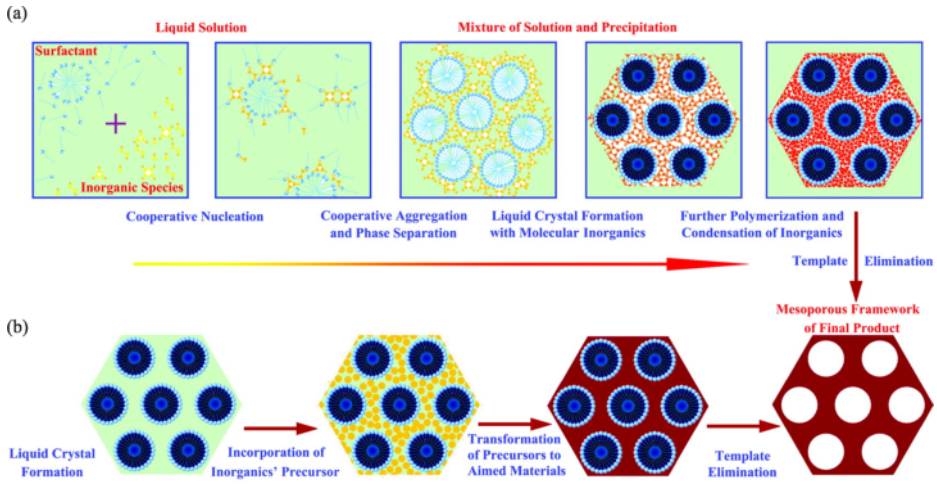

Fig. 2 (color online). Two synthetic strategies for the formation of mesoporous materials: (a) cooperative self-assembly; (b) "true" liquid-crystal templating process. Reprinted with permission from ref. [28]. Copyright 2007 American Chemical Society.

structures, a liquid crystal templating (LCT) mechanism has been discussed for some systems, which suggests that first a stable surfactant mesophase develops, around which the inorganic building blocks are assembled [14, 26, 27]. Both mechanisms are summarized in Fig. 2. The exact nature of the mechanism that occurs during thin film synthesis most probably depends on the chemical parameters and processing conditions, and often a combination of both mechanisms might operate.

Studies on the mechanism during film growth were also recently published by Jung *et al.* who reported on the *in situ* visualization of domain growth in the self-assembly of silica nanochannels using fluorescence

microscopy and atomic force microscopy (AFM) [29]. They observed well-ordered silica nanochannels with domain sizes of up to ∼0.3 mm and showed that the formation of transient lamellar structures precede the appearance of hexagonal layers. Furthermore they discussed that the layer growth follows two distinct pathways (for details see ref. [29]).

Thin Film Deposition and Functionalization Techniques

There are several techniques available for the preparation of thin films, of which a selection is depicted schematically in Fig. 3 [30]. Out of these, the EISA process described above is compatible with the chemical solution deposition methods, *i. e.* spin-coating, dip-coating, spray-coating, and meniscus-coating. These are widely employed, because they are cheap and do not require expensive and sophisticated equipment, but rather rely on techniques that are already commonly used in industrial processes. Moreover, they offer a good degree of control over the experimental conditions before and during the self-assembly process.

However, these methods usually do not result in a macroscopic in-plane alignment of the mesopores, most probably due to the lack of a preferential direction during the self-assembly process. Since there are many applications that could greatly benefit from mesopore alignment on a macroscopic scale, such as nanofluidics and nanoreactors [31], oriented growth of nanowires [32], and optoelectronic devices [33], a lot of effort was put into developing methods that can help achieving this goal. These methods include the use of microtrenches [34, 35], external electric [36, 37] and magnetic [38] fields, substrate surface modification [18, 39, 40], and shear flow control [41, 42]. However, these approaches often require specialized equipment or impose constraints on the applicable substrates or surfactants. That is why we recently investigated another technique, namely guided growth in PDMS microchannels [43], which will be discussed in more detail later in this review.

Wu *et al.* [34] and Daiguji *et al.* [35] demonstrated that microtrenches that introduce a spatial confinement during the EISA process can influence the mesopore alignment. The trenches were produced by top-down lithographic methods either by directly using

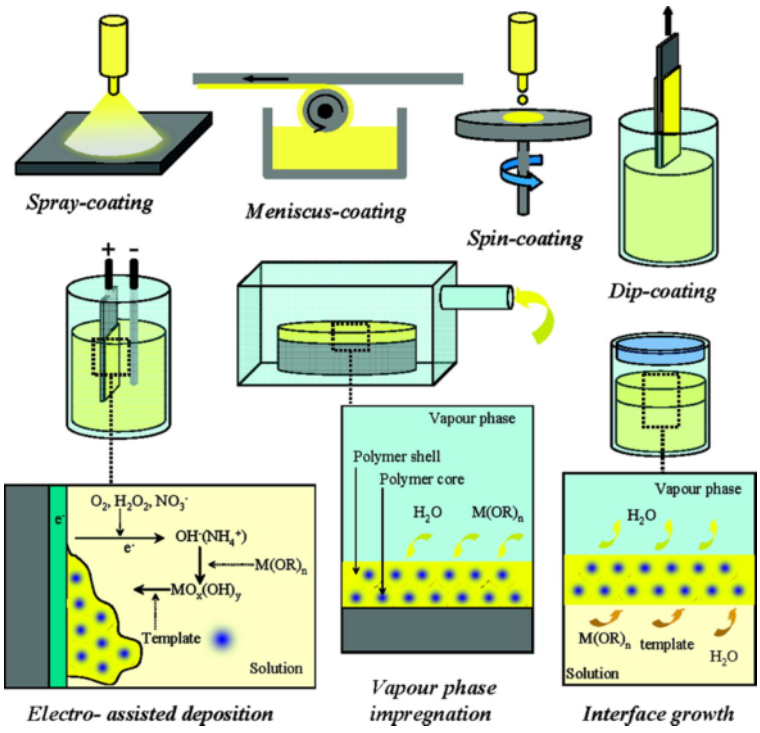

Fig. 3 (color online). Various processing methods used to prepare mesostructured thin films. Reprinted with permission from ref. [30]. Copyright 2008 American Chemical Society.

the pattern generated from the resist [34], or by transferring the pattern into the substrate *via* reactive ion etching [35]. In both cases, the spatial confinement led to a preferential alignment of mesopores inside the trenches. Wu *et al.* showed in their studies that the alignment depends critically on the aspect ratio of the microtrenches, while Daiguji *et al.* also found an influence of the composition of the precursor solution, the relative humidity during coating and aging, and the chemical properties of the trench sidewalls on the mesopore alignment. However, both methods require a clean room and a photolithography or even an electron beam lithography setup, rendering these approaches costly and time-consuming. Trau et al investigated the use of electric fields to induce mesopore alignment [37]. The authors used strong electric fields in combination with a microfluidic system to achieve mesopore alignment. They attributed the alignment effect to both the confined geometry and the presence of the electric field. However, the necessity of strong electric fields at the order of 1500 V/cm might limit the applicability of the technique. Furthermore, it also narrows down the choice of the substrate to non-conducting materials and the choice of the template to charged or ionic surfactants, typically resulting in mesoporous silica thin films with small pore sizes. Tolbert *et al.* demonstrated that magnetic fields instead of electric fields could also be used to trigger mesopore alignment [38]. They oriented a silicate-surfactant liquid crystal phase in an 11.7 T magnetic field by heating the samples above their anisotropic-to-isotropic phase transition temperatures, followed by slow cooling (5° C per hour in 3° to 5° steps) in the magnetic field and subsequent polycondensation of the silica by acidic or acidic-thermal treatment. While this approach also allows for a perpendicular alignment of the mesochannels with respect to the substrate plane, it requires very specialized equipment. Another approach was pursued by Yang *et al.* and Miyata *et al.*, who deposited thin silica films on mica [18] or single-crystal silicon wafers [39] and found that the crystallographic orientation of the substrate surface can influence the mesopore alignment to a certain degree. Miyata *et al.* also suggested another way to introduce mesopore alignment by substrate surface modification, namely by creating a thin polyimide layer on the substrate and subjecting it to a rubbing treatment that can help to align the polymeric chains [40]. This alignment is passed on to the micellar structure of the surfactant molecules and can lead to a macroscopic alignment of the mesopores. The exact formation mechanism that leads to the alignment seems to depend on the matching of the chain length of the hydrophobic part of the surfactant to the chemical structure of the polyimide underlayer [44, 45]. Zhao *et al.* [41] and Naik *et al.* [42] demonstrated that the shear flow exerted on films during dip coating can also influence mesopore alignment to some degree, but the correlation length of the obtained mesostructure might be low in these cases.

Besides macroscopic ordering and mesopore alignment, chemical functionalization of the pore walls of the porous materials is of great importance for many applications, since these determine the host-guest interactions of the system [46–48]. There is a large variety of synthesis strategies that lead to functionalized porous materials [30], of which the co-condensation approach and the chemical grafting approach will be briefly discussed here. In the co-condensation approach, organically modified building blocks (such as functionalized aryl or alkyltriethoxysilanes) are mixed with the inorganic building blocks and the templates in a one-pot reaction [49, 50]. During the self-assembly process, the functionalized silica species will hydrolyze and condense together with the other inorganic silica precursors, resulting in a random incorporation into the silica framework. Another commonly used approach is the post-synthetic grafting of organically modified silica species onto the porous materials. In this approach, the unfunctionalized porous material is first obtained with a standard synthesis protocol, and subsequently subjected to treatment with silica species that bear functional groups and that exhibit reactivity towards the free hydroxyl groups present at the surface of the silica pore walls. While the co-condensation approach is simpler and has the advantage of a more homogeneous distribution of the functional groups within the material and its channels, the presence of functionalized silica species during the synthesis can interfere with the delicate formation mechanism of the porous structure and may result in a less well-defined (or, at high loadings, a completely amorphous) material with reduced hydrothermal stability [51].

Characterization of Host-Guest Interactions with Single Molecule Microscopy Techniques

Knowing the interactions between the mesoporous host and the guest molecules is essential for many

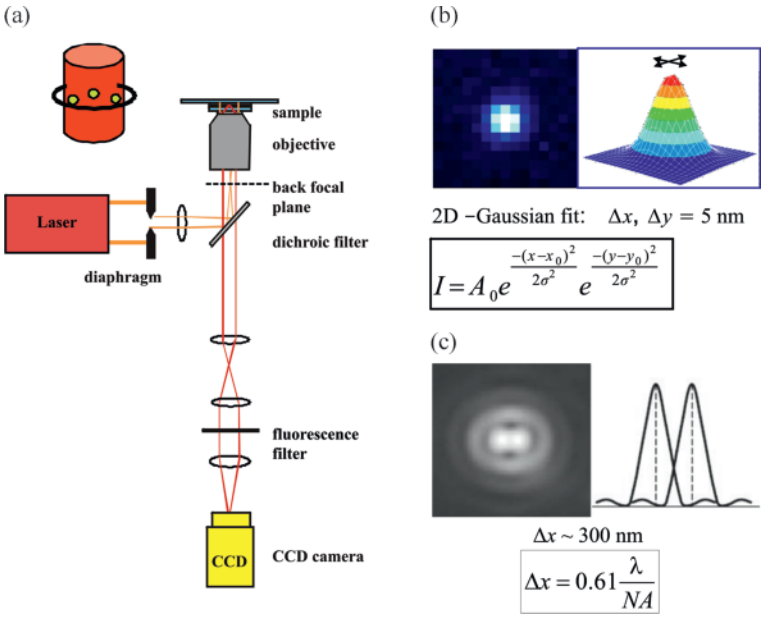

Fig. 4 (color online). (a) Schematic setup of wide-field epi-fluorescence microscopy (the cylinder depicts the excitation volume of the microscope). (b) The fluorescence intensity distribution of a single molecule can be fitted by a 2-dimensional Gaussian curve according to the equation. The peak position x_0 and y_0 can be determined with an accuracy down to typically 5 nm or less. (c) Demonstration of the Rayleigh criterion that describes the smallest distance Δx of two objects that can still be resolved by the optical system.

applications. To investigate these interactions, single molecule microscopy (SMM) is a powerful technique. While measurements of ensemble diffusion of molecules in porous hosts provide information about the overall behavior of the guest in the host, tracking of individual molecules provides insights into the heterogeneity and the mechanistic details of molecular diffusion as well as the structure of the host. In our SMM experiments we have shown how single dye molecules can be used as nanoscale probes to map out the structure of mesoporous silica channel systems prepared as thin films *via* the cooperative self-assembly of surfactant molecules with polymerizable silicate species [52, 53]. The dye molecules act as beacons while they diffuse through the different structural phases of the host: the structure of the trajectories, the diffusivities and the orientation of single molecules are distinctive for molecules traveling in the lamellar and the hexagonal mesophases [54]. These experiments reveal unprecedented details of the host structure, its domains and the accessibility as well as the connectivity of the channel system. In our studies, we mostly used strongly fluorescent and photostable molecules, *e. g.* terrylenediimide (TDI) derivatives, which can be easily incorporated into mesopores and then individually observed travelling in the host.

The idea that a single molecule can act as a direct reporter of its environment was pioneered in 1989 by Moerner [55] and Orrit [56], who were the first reporting on the optical detection of single fluorophores in a solid matrix at liquid-helium temperatures. Since then, single molecule microscopy (SMM) has been continuously improved (*e. g.* adapting it to room temperature) and now plays a growing role in chemistry, biology, physics, and materials science [57 – 61]. In the following, the basic principles of SMM will be explained.

Principles of Single Molecule Fluorescence Microscopy

Nowadays, there are different types of microscopes available for single molecule experiments, such as confocal, total internal reflection fluorescence (TIRF) or wide-field epi-fluorescence microscopes. All these techniques are based on the detection of fluorescence light, which can provide an excellent signal-to-noise (or signal-to-background) ratio. In this review we focus mainly on studies that employ wide-field epi-fluorescence microscopy (schematic setup see Fig. 4a). The samples are excited with a laser beam that is focused on the back focal plane of the microscope objective: this results in a cylindrical excitation volume, depicted in Fig. 4a. Since the concentration of the fluorescent dye molecules is kept extremely low ($\leq 10^{-10}$ M), single molecules can be detected by their individual

fluorescence spots imaged onto the CCD camera. The imaging is done with an objective with a high numerical aperture ($NA = 1.4$). The numerical aperture NA is defined as:

$$NA = n(\sin\alpha)$$

with n being the refractive index of the medium (*e. g.* oil) in which the objective lens is working, and α the half collection angle of the objective. The higher the NA, the higher is the light collection efficiency of the objective and thus the number of the collected photons. The emitted fluorescence passes a dichroic mirror and a fluorescence filter to get separated from the exciting laser wavelength. The signal is detected by a back-illuminated, cooled electron multiplying charge-coupled device (EMCCD) camera. The position of a single molecule which acts as a point light source can be determined by fitting a 2-dimensional Gaussian distribution (Fig. 4b) to the signal on the detector chip, according to

$$I = A_0 e^{\frac{-(x-x_0)^2}{2\sigma^2}} e^{\frac{-(y-y_0)^2}{2\sigma^2}}$$

where I is the recorded fluorescence intensity, A_0 the amplitude of the signal and σ the width of the Gaussian curve. x_0 and y_0 are the coordinates of the peak position. The position accuracy corresponds to the standard error of the fitting parameters x_0 and y_0 and depends on the photon noise, the error due to the finite pixel size of the detector and the background. Moreover, the position accuracy depends on the fluorescence intensity of a single molecule since Δx is inversely proportional to the square root of the number of collected photons. Thus, in SM experiments one tries to get as many photons as possible from a single fluorescent molecule. This can be achieved by the use of the proper optical system as described above, as well as by using molecules with high fluorescent quantum yield and high photostability so that they can be excited with high excitation intensities. In this way the position of a single fluorescent molecule like TDI can be determined with an accuracy of typically 5 nm or less.

This striking resolution needs to be clearly distinguished from the resolution of the microscope that describes the smallest distance Δx of two objects that can still be distinguished from one another (see Fig. 4c). This distance is roughly equal to the full width at half maximum of the signal and is given by Abbe's law and the Rayleigh criterion (Fig. 4c). It follows that the higher the NA, the smaller the minimum distance Δx of two objects that can be resolved. By using visible light (*e. g.* 633 nm), the lateral resolution is about 300 nm. SMM, however, overcomes this resolution limit, since the samples in these studies are prepared on a single molecule level, meaning a very low fluorescent dye concentration (of about 10^{-10} to 10^{-11} M) as mentioned above. Hence, the probability of two molecules coming closer than 300 nm to each other is very low.

In order to investigate the diffusion behavior of single molecules incorporated into porous hosts, movies of many images in time series (*i. e.* frames) were collected. Then, the position of the molecules was determined in each individual frame and connected frame-by-frame to give a SM trajectory. This trajectory gives detailed information about the pathway of the molecule within the pores and thus the structure of the host. Such movies can be found in the Supplementary Material of articles by Kirstein *et al.* [53] or Zürner *et al.* [52].

Structural Analysis by Combining TEM and SMM Studies

To learn more about host-guest interactions, *e. g.* how a single fluorescent dye molecule travels through linear or strongly curved regions of a mesoporous channel system, a combination of electron microscopic mapping and optical single-molecule tracking experiments was performed by Zürner *et al.* [52]. In this study, an extremely thin mesoporous silica film with a 2D-hexagonal pore arrangement and a pore to pore distance of about 7 nm was synthesized on a silicon nitride membrane (Si_3N_4 membrane). In order to correlate fluorescence and structural features, a fluorescent terrylenediimide (TDI) derivative and 280 nm polystyrene beads were added to the synthesis solution of the mesoporous silica. The polystyrene beads were used as markers and allowed the authors to overlay the transmission electron microscopy (TEM) images with the SMM images. Fast Fourier transform (FFT) directors obtained from a FFT analysis of regions in the TEM images (black bars in Fig. 5a) indicate parallel aligned channels with strongly curved areas and domain boundaries. By overlaying the SM trajectory over the TEM images it can be clearly seen that the molecule diffuses along the pores. This was the first direct proof that the molecular diffusion path-

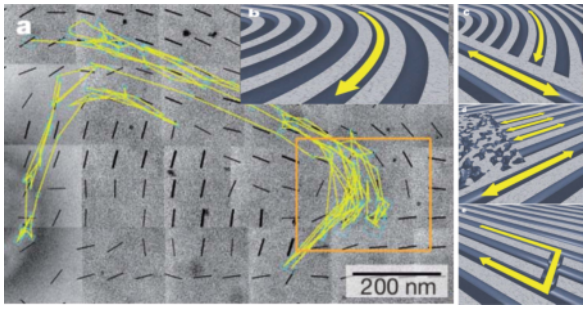

Fig. 5 (color online). (a) Overlay of a single-molecule trajectory (yellow) and multiple TEM images of the silica film (grey) stitched together to provide a macroscopic overview of the sample. The pathway of the molecule is influenced by the domain architecture of hexagonally ordered mesoporous silica pores. Domain boundaries and the local orientation of the pores (black bars) are indicated by the fast Fourier transform of the TEM images. (b–e) Schematic representations of structural elements and molecular movements found in hexagonal mesoporous silica films. Figures adapted from ref. [52].

way through the pore system correlates with the pore orientation of the two-dimensional hexagonal structure (Fig. 5). Changes of the molecular diffusional movement (and even stopping at less ordered regions) in the channel structure, repulsion by domain boundaries with different channel orientations, or lateral motions between 'leaky' channels allow a molecule to explore different parallel channels within an otherwise well-ordered periodic structure. This striking heterogeneity of diffusion behavior only becomes apparent through single molecule experiments, whereas TEM provides static information only. Moreover, TEM images correspond to an average over the thickness of the film, and while giving a good indication about the general local architecture, they cannot show single defects such as closed channels or open neighboring channels, which can be detected by SMM. In a subsequent study, we applied the knowledge that SMM can characterize the structural properties of the mesoporous structure in a non-invasive and direct way and optimized the synthesis conditions that lead to porous silica thin films with highly oriented mesopores.

Applications of SMM to Optimize and Analyze the Pore Alignment in Mesoporous Silica Thin Films

The aim of a recently published work by Rühle *et al.* [43] was to find a synthesis strategy that allows for synthesizing 2D-hexagonal mesoporous silica thin films with highly oriented and parallel aligned mesopores over large domains (Fig. 6c). For this study, an immediate feedback about the mesoporous structure was obtained from SMM. Fluorescent TDI dye molecules were added to an EISA precursor solution (containing tetraethylorthosilicate (TEOS), Pluronic F127, ethanol, HCl and water) and incorporated into the channels at single molecule concentrations (see schematic representation in Fig. 6a). The task of the dye molecules is to explore and map out the possible pathways within the mesoporous channel network in a non-invasive way. This is done by recording a movie at the desired position of the sample with a fluorescence microscope and subsequently reconstructing an image in which each pixel assumes the maximum value it reaches in the individual frames. Hence, the fi-

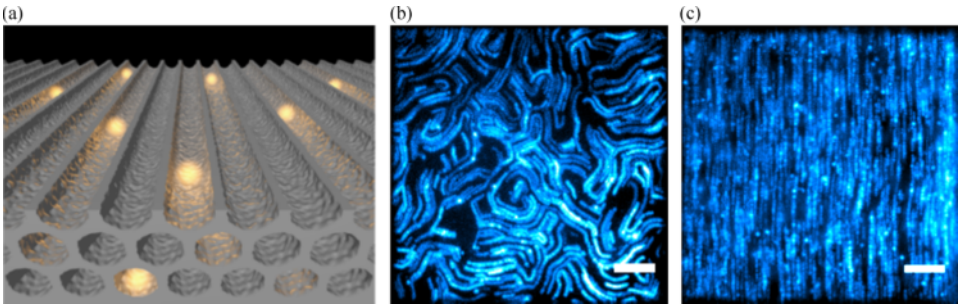

Fig. 6 (color online). Single molecules moving through silica mesopores. (a) Schematic representation of fluorescent dye molecules diffusing inside 2D-hexagonally arranged mesopores of a porous silica host (the template is omitted for clarity). (b–c) Maximum projections of the individual frames of a wide-field movie taken from the mesoporous silica material with b) non-aligned pores lying in a plane parallel to the substrate and c) with aligned pores, lying in a plane parallel to the substrate and showing a preferential alignment on a macroscopic length scale. Scale bars are 5 μm. Reprinted with permission from ref. [43]. Copyright 2012 American Chemical Society.

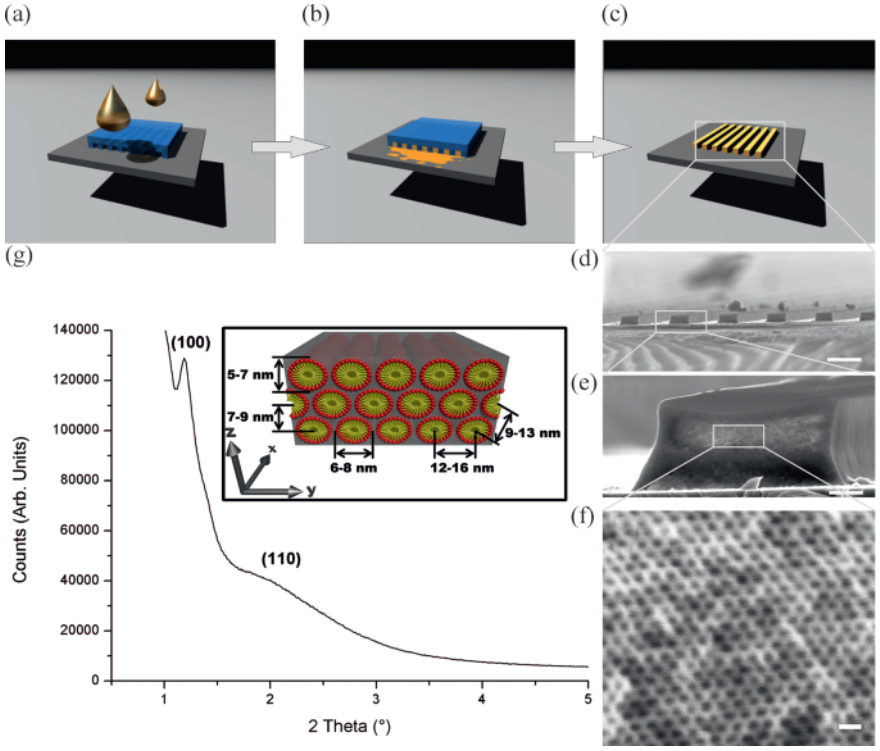

Fig. 7 (color online). Schematic presentation of the synthesis of thin silica films with highly oriented mesopores and structural analysis of the mesopore system. The EISA precursor solution is placed on a glass coverslip close to the open ends of a PDMS stamp (a) and pulled into microgrooves of the PDMS stamp by capillary forces (b). After solidification of the solution, the PDMS stamp is removed to obtain the mesoporous silica pattern (c). SEM image of the mesoporous silica pattern (d). Magnified image of a silicon bar (e). Cross-sectional HR-SEM images (cleaved perpendicularly to the long axis of a silicon bar) of mesoporous silica (f). XRD pattern and schematic illustration of the dimensions of the mesoporous silica material (g). Reprinted (adapted) with permission from ref. [43]. Copyright 2012 American Chemical Society.

nal image consists only of the brightest pixels of the movie. This technique (called a "maximum projection") treats moving and stationary fluorescent objects more equal than simply averaging over all frames of the movie [43]. Two examples of such maximum projections are depicted in Figs. 6b and 6c. One can immediately see whether the structure of the synthesized silica mesopores is random (Fig. 6b) or well-aligned (Fig. 6c).

To create thin silica films with highly oriented mesopores, the authors applied a technique known as micromolding in capillaries (MIMIC) [36, 37] in which an EISA precursor solution is filled into a confined space (microgrooves) defined by a poly(dimethylsiloxane) (PDMS) stamp. The solution is placed at both ends of the PDMS stamp (Fig. 7a) and gets sucked into the microgrooves by capillary action (Fig. 7b). After solidification of the structure, the stamp can be carefully peeled off (Fig. 7c). Rühle *et al.* varied different experimental parameters to investigate their influence on mesopore alignment, *e. g.* the height-to-width ratio of the microgrooves, the surface modification of the stamp and the substrate, as well as the synthetic conditions during solidification of the silica framework, Modification of the stamp influences the solid/liquid interface at three side walls of the resulting microgrooves, while modification of the substrate influences one solid/liquid interface. The best results were achieved by using substrates rendered hydrophilic by exposure to oxygen plasma, in combination with hydrophobic, untreated PDMS stamps and a slowed-down solidification of the silica matrix in the presence of an ethanol atmosphere. The structure of the mesoporous silica in the microgrooves

was also determined by using standard characterization methods like small-angle X-ray scattering (SAXS) and cross-sectional high-resolution scanning electron microscopy (HR-SEM) (Fig. 7d). Both provide evidence for hexagonally arranged mesopores lying in a plane parallel to the substrate. The cross-sectional HR-SEM images (cleaved perpendicular to the microgroove direction) also indicate the well-ordered state of the mesopores along the long axis of a microgroove. The elliptical shape of the mesopores (Fig. 7f) is due to the anisotropic shrinkage in mesoporous silica films during drying. Image analysis of the HR-SEM data gives a mean mesopore width of 6 – 8 nm and a height of 5 – 7 nm, and a pore-to-pore distance of 12 – 16 nm horizontally and 9 – 13 nm diagonally, which is in line with the *d* spacing of the XRD (100) peak of about 7.5 nm (Fig. 7g) [43].

While these standard methods can give insights into the mesoporous structure and the pore directionality of the silica host, they either give only averaged data for a certain area without spatial resolution or they can only extract this information for a small fraction of the silica film. To gain more detailed information about the domain size and correlation length of the cylindrical mesopores, the defects in the silica walls, and the dead ends of the channels, it is necessary to characterize the movement of the guest molecules by single molecule tracking and analyze the trajectories in detail. To improve the positioning accuracy, concentration of the molecules was further decreased which resulted in a better signal-to-noise ratio and allowed positioning accuracies in the range of 6 – 8 nm. This value is smaller than the horizontal pore-to-pore distance (12 – 16 nm, see also the schematic illustration of the dimensions of the mesoporous silica material in Fig. 7g) and hence made it possible to precisely localize dye molecules and to distinguish their position from the position in a neighboring channel. The maximum projection and the trajectories of the analyzed sample are shown in Figs. 8a and 8b. Exemplarily, trajectory no. 1 was enlarged in Fig. 8c, showing that it extends about 4 μm in the channel direction, which is chosen as the *x* direction. In *y* direction however, it varies its width, being broad in the top region and thinning out towards the bottom region. The *y* axis is enlarged into the nanometer range while the *x* axis is kept in the micrometer range. The resulting graph clearly shows four different, distinguishable regions in *y* direction, marked with different colors. From the *x*-*y* plot of the trajectory in Fig. 8c, the two separate graphs *x*(t) and *y*(t) can be obtained (see Figs. 8d and 8e). These graphs depict the movement of the molecule as a function of time separated in *x* and *y* direction. The time dependence of the *y* coordinate in Fig. 8e demonstrates that the molecule jumps in the *y* direction in four consecutive steps. The distances of these jumps can be correlated to jumps between adjacent channels. The corresponding channel structure is shown in Fig. 8f. With this figure the jumps of the molecule from region 1 (black) to region 4 (green) can be clearly interpreted as switches between adjacent channels. So the molecule starts in channel 1 and then jumps after 31.6 s into an adjacent channel 2 where it then moves for an additional 93.9 s. Then it jumps again through an adjacent channel into channel 3 and stays there for additional 39.2 s to finally jump into channel 4. Additional information can be obtained from the graph *x*(t) in Fig. 8d. This plot shows the movement of the molecule for 165 s between two dead ends within a range of 1.5 μm. Interestingly, these dead ends seem to be nearly at the same position in *x* direction for the first two channels and may change somewhat for the third channel. After 165 s the molecule switches into channel 4 which extends further in *x* direction for more than 2.5 μm. Hence, the defects in the walls of the mesopores are crucial to enable the molecules to move through the entire mesoporous structure. This example demonstrates how important SMM is to reveal the *real structure* of the mesoporous system including its most relevant defects.

Mesoporous Silica Filaments as Hosts for Biomolecules

A further approach to control the mesoporous structure is the confined synthesis of mesoporous silica inside porous anodic alumina membranes [48, 62, 63] *via* the EISA process. Feil *et al.* [48] synthesized template-free, chemically functionalized mesoporous silica filaments with 4 nm pore diameter and used SMM to investigate the translational and orientational dynamics of TDI dye molecules (see chemical structure in Fig. 9) and dye-functionalized (Cy3 and Cy5) double-stranded DNA (ds-DNA). In order to introduce a homogeneous chemical functionalization of the porous host with nitrile groups (10 mol-% with respect to the silica source), a co-condensation of the silica ma-

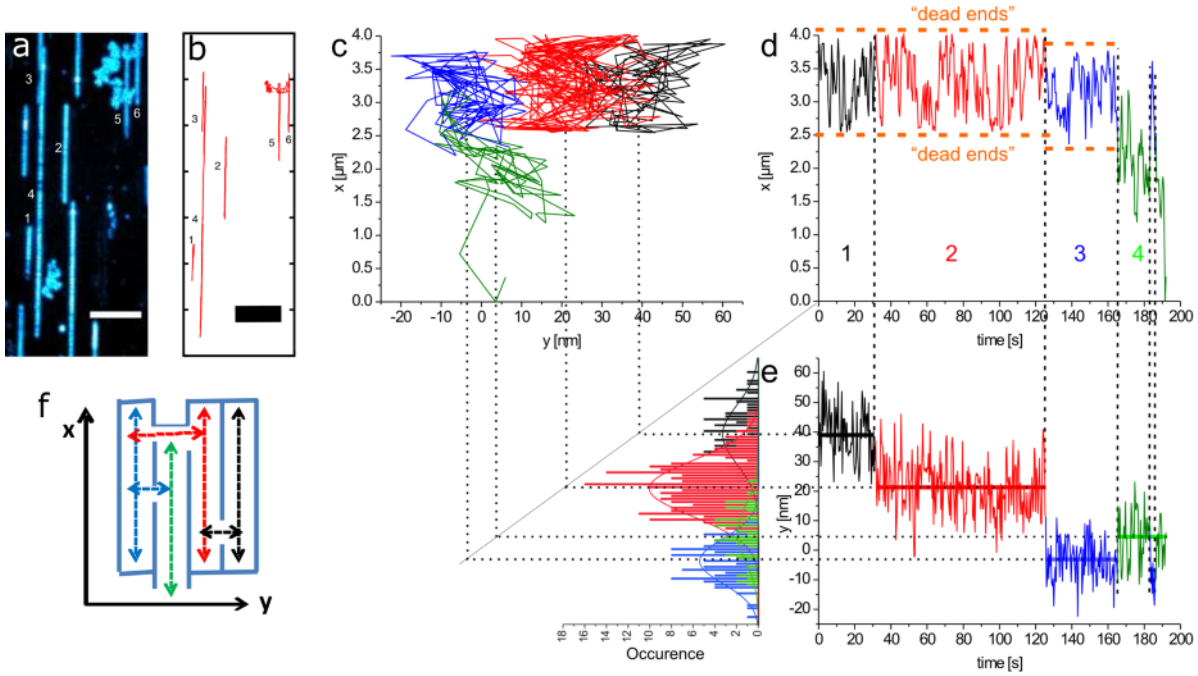

Fig. 8 (color online). Analysis of trajectories in aligned mesopores. Maximum projection (a) and trajectories (b) revealing the pathways of single molecules in the mesoporous structure. The mesopores lie in a plane parallel to the substrate and show a preferential alignment on a macroscopic length scale (scale bars are 5 μm). Trajectory of molecule no. 1 with the *y* axis in the nanometer range and the *x* axis in the micrometer range for better clarity (c). Projection of *x* and *y* coordinates as a function of time for the single molecule shows diffusion in at least four distinct neighboring pores (marked with black, red, blue, and green), while the molecule moves back and forth in each pore. Histograms of the *y* lateral coordinate (bottom left) for the four different time intervals with their Gaussian fits (black, 42.8 ± 1.0 nm; red, 24.6 ± 0.7 nm; blue, 0.0 ± 0.7 nm; green, 7.5 ± 0.2 nm) (d, e). A schematic pathway of the single molecule, switching between neighboring channels (f). Reprinted (adapted) with permission from ref. [43]. Copyright 2012 American Chemical Society.

trix with (2-cyanoethyl)triethoxysilane was performed. The template was then removed by Soxhlet extraction. Afterwards, amino groups were grafted to the channel walls to favor the uptake of the negatively charged DNA constructs. The samples were loaded with the desired guest molecules at a concentration appropriate for single molecule studies.

First, TDI dye molecules were incorporated into nitrile-functionalized mesoporous channels and studied by SMM. While the TDI molecules remained immobile in the mesopores under air atmosphere, diffusion inside the pores could be detected in the presence of a saturated chloroform/water atmosphere acting as a lubricant phase. To ensure that the observed diffusion of single TDI molecules occurs in the mesoporous channels of the host material and not on the surface, a 0.4 nm thin layer of gold was deposited on the surface of the sample by thermal evaporation. This way, the fluorescence of all molecules on the surface of the glass substrate was quenched, and only molecules inside the mesoporous host remained fluorescent (Fig. 9a). Their positions could be correlated to the transmission optical images of the filaments (Fig. 9b). Furthermore, the trajectories of the molecules were highly structured due to the confinement in the columnar mesopores (Figs. 9c and 9d) and provided detailed information about the host structure, such as domain size (up to about 10 μm) and the presence of defects. The next step was to load DNA into mesopores. The functionalization of the pores and thus the interaction between host and guest turned out to play an important role for achieving this goal. The authors observed no loading in unfunctionalized or mono-functionalized mesopores, but only in bi-functionalized samples. The loading process took about 2 weeks, and movement of the DNA molecules was only detectable under a high hu-

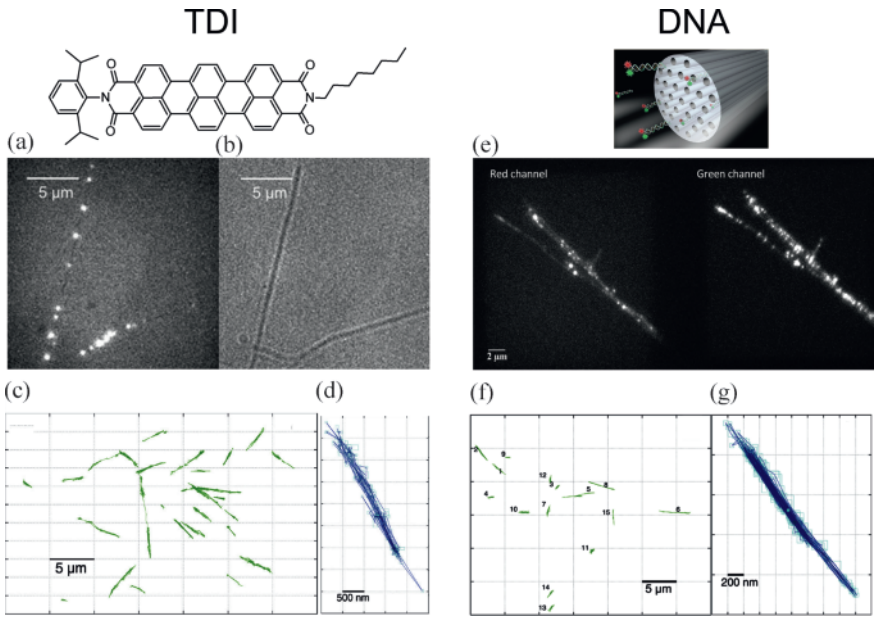

Fig. 9 (color online). Fluorescence image of single TDI molecules within filament channels (a). Molecules located on the cover glass are quenched with a coating gold layer. The positions of the bright spots are perfectly correlated with the structure of the filaments displayed in the optical transmission image (b). Overview of several linearly shaped single molecule trajectories (c). Example of a single TDI molecule trajectory (d). FRET experiment of Cy3-Cy5 labeled ds-DNA strands inside the mesoporous filaments structure (e). Left: red channel showing the red emission of fluorescing Cy5 molecules after FRET. This means that the ds-DNA strands are still intact. Right: green channel showing Cy3 fluorescence. Overview of several single molecule trajectories of ds-DNA strands (f). Example of a ds-DNA molecule trajectory (g). Reprinted (adapted) with permission from ref. [48]. Copyright 2012 American Chemical Society.

midity atmosphere. The DNA was labeled with Cy 3 (donor) and Cy 5 (acceptor) dyes to check its integrity by measuring the Förster resonance energy transfer (FRET) signal. FRET is strongly distance-dependent, and in the case of DNA denaturation, the two single strands will be separated and no FRET signal in the red channel is expected. Feil *et al.* [48] observed Cy3 fluorescence in the green channel (right) and emission of fluorescing Cy5 molecules upon FRET in the red channel (left) (Fig. 9e). This demonstrates that the ds-DNA strands were still intact after loading into the mesoporous channels. Furthermore the trajectories were highly structured and quite linear over up to 7 μm. In addition, the diffusion constant for ds-DNA and also for TDI was obtained by fitting the linear part of the plots of the mean square displacement (*MSD*) *vs.* time with the 1-dimensional form of the Einstein-Smoluchowski equation, $MSD = 2\,Dt$.

Fig. 10 shows the single molecule diffusion analysis of ds-DNA and TDI molecules in mesoporous filaments. The results indicate that while the larger DNA molecules took much longer to be loaded into the mesoporous channels compared to the smaller TDI molecules, they moved nearly as fast once they were inside the mesopores. The single molecule diffusion coefficients of the DNA molecules have a mean value of $\langle D \rangle = 5.9 \times 10^4\,\mathrm{nm^2\,s^{-1}}$ for saturated H_2O vapor pressure at room temperature, while TDI molecules have a diffusion constant of $\langle D \rangle = 1.1 \times 10^5\,\mathrm{nm^2\,s^{-1}}$.

This work has shown once more how important it is to investigate host-guest interactions with SMM to provide a solid basis for a thorough understanding of the interactions within a porous material. Furthermore, the right functionalization of the highly structured collinear pore walls clearly plays an important role for applications in bioanalytics and drug-delivery (see Outlook).

Diffusion in Thin Silica Films

Very interesting work on single molecule diffusion studies of different guest species in silica thin films was

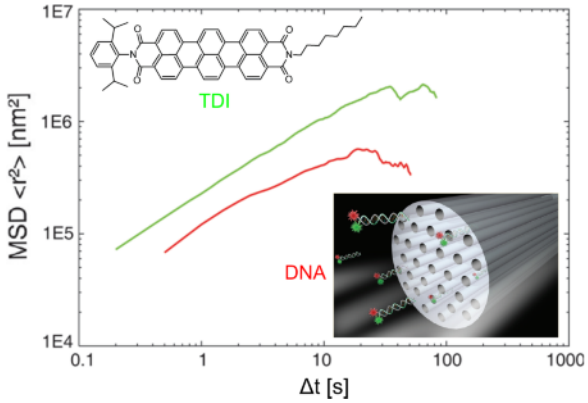

Fig. 10 (color online). Single molecule diffusion analysis of TDI and ds-DNA molecules in mesoporous filaments. Comparison of the average *MSD* plots of TDI (green) and ds-DNA (red) molecules. The *MSD*s of the DNA molecules are about two times lower than the *MSD*s of TDI. Furthermore, the difference in size of the observed guest molecule is reflected by the shape of their *MSD*s. While the mean *MSD* plot of the small TDI molecules is nearly linear (which suggests normal diffusion) over the observed time range, the mean *MSD* plot of the ds-DNA molecules bends for longer time intervals (due to the confined diffusion in the mesopores). This indicates that the larger DNA molecules respond more strongly to the confinement in the filaments than the TDI molecules. Reprinted (adapted) with permission from ref. [48]. Copyright 2012 American Chemical Society.

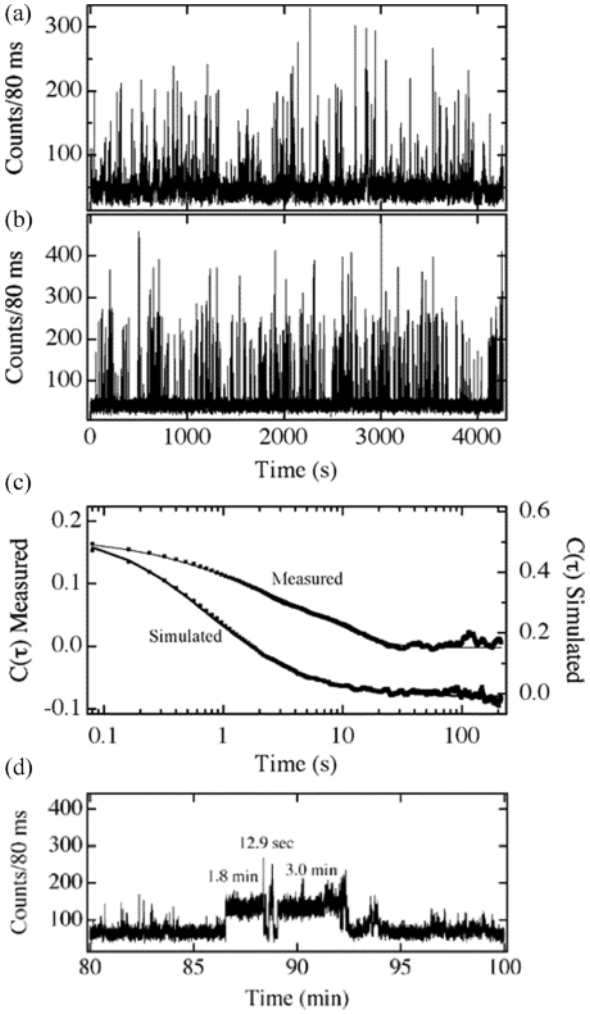

Fig. 11 (color online). (a) Representative fluorescence time transient recorded for Nile Red in an as-synthesized mesoporous silica film. (b) Simulated time transient obtained by using a molecular areal density of 0.6 molecules μm^{-2} and $D = 3 \times 10^{-10}\,cm^2\,s^{-1}$. (c) Autocorrelations (points) and fits (lines) for the data shown in parts a and b. (d) Expanded section of a representative time transient showing long-term adsorption events in an as-synthesized film. Each of the three designated events is labeled with the measured desorption time. Reprinted with permission from ref. [68]. Copyright 2006 American Chemical Society.

also done by Higgins *et al*. In early studies, they investigated the nanoscale properties, the heterogeneity, and the diffusion behavior of dye molecules in dense (organically modified) sol-gel silica films at the single molecule level [64 – 67]. Later, Fu *et al.* [68] and Ye *et al.* [69] extended the approach to porous silica thin films. By incorporating fluorescent dyes into the surfactant phase of the mesoporous silica thin films and comparing their diffusional movement to that of dye molecules loaded into template-free films after calcination, striking differences in the dynamics could be observed. The measurements revealed that the dye molecules were relatively mobile in the as-synthesized (*i. e.* surfactant-containing) films, but appeared to be entrapped at fixed locations after being loaded into the calcined (*i. e.* template-free) films. Upon rehydrating the calcined films under high humidity conditions, the dye molecules became mobile again. These results indicate that the surfactant phases of the as-synthesized material and the hydrated pores of the calcined material after exposure to high humidity behave like fluid-filled domains, providing a "lubricant" phase that enables mass transport of the dye inside the porous host. The authors used fluorescence imaging and single-point fluorescence time transients in their studies (see Fig. 11). These fluorescence correlation spectroscopy (FCS) methods are interesting for diffusion studies as they feature a high time resolution and hence al-

low for the investigation of rapid processes. Moreover, FCS measurements are independent of photobleaching which can limit the amount of available data from other techniques. However, no structural information on the porous host can be obtained, and a model for the possible mode of motion needs to be provided.

In contrast to those studies, we investigated the diffusional processes of various fluorescent dye molecules in the nanoporous network of sol-gel glasses [70] and in mesoporous materials [71] with the direct method of single molecule tracking. Furthermore we showed diffusional and orientational dynamics of various single dye molecules in nanostructured host-guest materials [72] and the switchable mobility of single TDI molecules in networks of long unidimensional nanochannels [73]. In these studies, a more direct observation of the mobility of the dye molecules could be achieved by the optical tracking and polarization techniques than in the FCS studies of Higgins *et al.* [64 – 69].

Diffusion Phenomena, Morphology, Intergrowth and Accessibility in Porous Catalyst Particles

Investigations of diffusion processes and identifying diffusion barriers for molecules inside porous compounds play a major role in many heterogeneous catalysis processes. If the intraparticle diffusion is too slow or if there are substantial diffusion barriers, a depletion of substrate molecules can occur, and only a fraction of the catalytically active particle is actually used. Hence, visualizing, measuring and quantifying diffusion processes is crucial to provide a better understanding and to make a rational design and improvement of the porous catalysts possible. De Cremer *et al.* showed how single molecule fluorescence spectroscopy could be used to visualize and quantify the effects of mass transfer limitations on the overall catalytic efficiency in a spatially resolved fashion [74]. As a model system, the authors chose mesoporous Ti-MCM-41 particles which catalyze the epoxidation of a fluorescent dye (PBD-bodipy), resulting in a spectral shift of the excitation and emission maximum of the products. Hence, the emission of the reaction products could be spectrally separated from the educts, and single turnover events could be subjected to a spatial and temporal analysis (see Fig. 12), giving quantitative information about the catalytic process.

Karawacki *et al.* showed that the decomposition of template molecules in zeolite-type crystals yields light-absorbing and fluorescent intermediates, which they used to elucidate the 3-dimensional intergrowth structure by means of *in-situ* optical and fluorescence microscopy during heating [75]. In another study, also by Karawacki *et al.*, the authors related the intergrowth structure of zeolites to internal and outer-surface molecular diffusion barriers [76]. In their study, they used a combination of confocal fluorescence microscopy, electron backscatter diffraction from samples prepared by focused ion beam sectioning, transmission electron microscopy imaging and diffraction, atomic force microscopy, and X-ray photo-

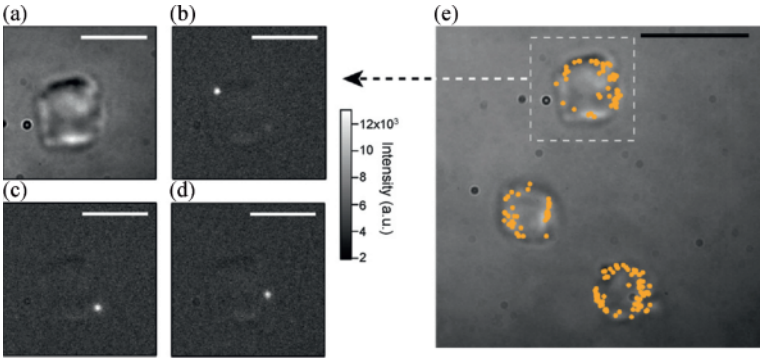

Fig. 12 (color online). (a) Transmission image of an individual Ti-MCM-41 particle. (b–d) Three representative examples of fluorescent bursts due to the formation of a single product molecule in the Ti-MCM-41-catalyzed epoxidation of the PBD-bodipy probe. The white scale bars in panels a–d represent a distance of 3 μm. (e) Transmission image of three Ti-MCM-41 particles on which the positions where reactions were observed over a time span of 140 s are highlighted by a yellow mark. The black scale bar represents a distance of 5 μm. Reprinted with permission from ref. [74]. Copyright 2010 Elsevier.

electron spectroscopy to study a wide range of coffin-shaped MFI-type zeolite crystals, and presented an overview of the morphology-dependent MFI-type intergrowth structures. Sommer *et al.* used a Brønsted acid-catalyzed oligomerization of styrene derivatives to study the intergrowth structure and the active site accessibility in etched SSZ-13 zeolites by confocal fluorescence microscopy [77]. The authors found a high degree of heterogeneity in the density of defects and the catalytic activity among different crystals within one SSZ-13 batch.

Catalytic Reactivity Mapping in Porous Silica Compounds

Another interesting application of single molecule spectroscopy is the mapping of catalytically active sites within porous materials. Roeffaers *et al.* used the liquid phase acid-catalyzed self-condensation of furfuryl alcohol in dioxane as a reporter reaction for imaging the catalytic activity of active sites in individual zeolite crystals [78, 79]. After the condensation of the furfuryl alcohol, the reaction products entrapped in the pores are sufficiently fluorescent to be detected with a confocal microscope. When polarized excitation light is used, the efficiency of excitation and emission is strongly orientation-dependent since the linear oligomeric products have transition dipole moments of absorption and emission parallel to the long molecular axis. This anisotropy allows conclusions about the orientation of the emissive product molecules and hence the channel orientations within the zeolite crystals [78]. In another study, Roeffaers *et al.* demonstrated the use of the same self-condensation reaction to study the reactive sites within ZSM-22 and ZSM-5 crystals with a new technique they called NASCA (nanometer accuracy by stochastic catalytic reactions) microscopy [79]. In this technique, 2D-Gaussian functions are fitted to the (diffraction-limited) emission spots of the fluorescent product molecules, and from these data, a high-resolution image is reconstructed that gives valuable information about the catalytic activity at different locations within the crystal (see Fig. 13).

Kox *et al.* investigated the catalytic conversion of various thiophenes over individual ZSM-5 crystals, using a combination of X-ray absorption, UV/Vis and fluorescence microspectroscopy [80]. The authors discuss the effect of spatial heterogeneities on product

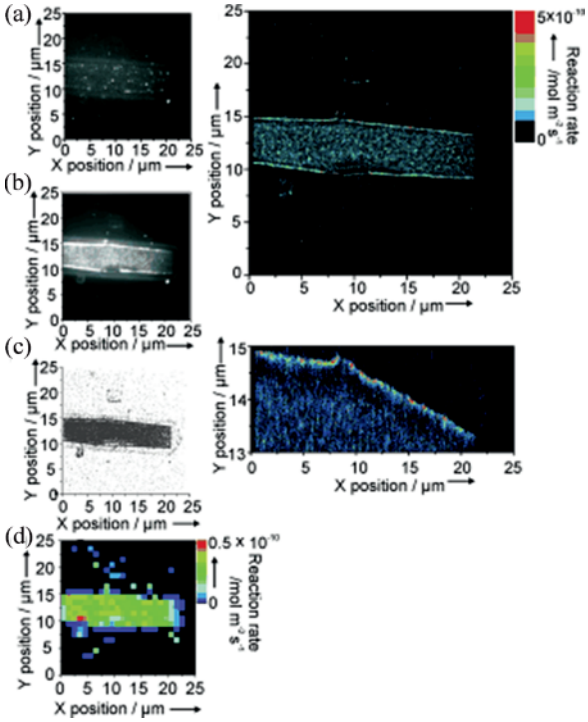

Fig. 13 (color online). (a) Individual fluorescent product molecules on/in a ZSM-5 crystal. The contours of the crystal are visible because of a small amount of unfiltered scattered light. (b) Accumulated and diffraction-limited image of all reactions observed during the time course of the recorded movie (80 s, 800 frames). (c) Reconstructed image obtained after mathematical fitting of all reaction events observed in the 800-frame movie. (d) Resolved reaction map ($1 \times 1\ \mu m^2$) reconstructed using the data in (c). (e) Similar resolved reaction map (top) calculated for $20 \times 20\ nm^2$ pixels with a zoom (bottom) at the upper part of the active rim. Reprinted with permission from ref. [79]. Copyright 2009 Wiley-VCH.

formation and the alignment of distinct reaction products within the pores, and visualize the 3D distribution of reaction products within the crystals, showing the influence of crystal intergrowth and concurrent diffusion barriers. Chung *et al.* studied the coke formation during the aromatization of paraffin and olefin hydrocarbons over ZSM-5 in a space and time-resolved manner [81]. In this study, polarization dependent *in situ* UV/Vis micro-spectroscopy and confocal fluorescence microscopy were used to show how large polyaromatics mainly grow in alignment with the zeolite straight channels and how these techniques can be used to reveal spatial heterogeneities of the photo-excited coke compounds. Buurmans *et al.* used Nile Blue

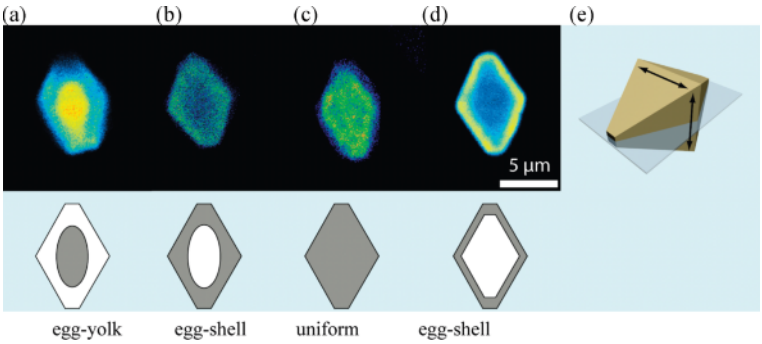

Fig. 14 (color online). Fluorescence intensity maps of an individual H-Beta zeolite crystal recorded with a laser excitation of 488 nm (detection at 510 – 550 nm). Samples were taken after 3 h of reaction at 140 °C with (a) glycerol, (b) ethylene glycol, (c) 1,3-propylene glycol, and (d) 1,2-propylene glycol. (e) Schematic representation of the slice at which the confocal fluorescence measurements were performed, with the arrows indicating the direction of the pores. Reprinted with permission from ref. [89]. Copyright 2010 American Chemical Society.

A and a Brønsted acid-catalyzed thiophene oligomerization that yields a fluorescent product to selectively stain different components and investigate Brønsted acidity and catalytic activity in fluid catalytic cracking (FCC) particles [82], while Karreman *et al.* used a fluorostyrene oligomerization (also yielding a fluorescent product) in an integrated laser and electron microscopy study to investigate and characterize these industrially important catalysts [83]. Stavitsky *et al.* also used fluorescence generated through oligomerization of various styrene derivatives for time- and space-resolved optical and fluorescence investigations of the shape selectivity and catalytic activity within the pores of ZSM-5 crystals [84], and Kox *et al.* used a styrene oligomerization reaction in a combined *in-situ* optical and fluorescence microscopy study of ZSM-5 featuring micro- and mesoporosity (introduced through desilication) for investigating the intergrowth structure and catalytic activity trends [85]. Domke *et al.* introduced a technique for tracing catalytic conversion on single zeolite crystals in 3D with nonlinear Raman- and two-photon spectromicroscopy [86]. The authors used these techniques to gain mechanistic insights into the alkene activation and glycol etherification catalyzed by large crystal H-beta zeolites.

Catalyst Deactivation

Catalyst deactivation is a very important issue in industrial processes. One of the most important deactivation mechanisms in acid heterogeneous catalysis, and for zeolites in particular is a deactivation due to coke formation. In this process, heavy by-products that are formed during the catalytic reaction cover the active sites or block the pore network of the zeolite, resulting in a partial or total loss of catalytic activity. Fluorescence microscopy in combination with other techniques can help to obtain a more detailed picture of the individual processes that happen inside the pores of porous materials employed in industrial applications. Ruiz-Martinez *et al.* studied the deactivation process of FCC catalyst particles containing zeolite Y or ZSM-5 by sulfur compounds [87], and Mores *et al.* investigated the deactivation of H-ZSM-5/silicalite-1 zeolite composites [88]. Parvulescu *et al.* focused on another important industrial process, namely the etherification of biomass-based alcohols with olefins over beta zeolites [89]. Confocal fluorescence microscopy studies allowed the authors to observe the interaction between the reactants and the catalyst particles in a space-resolved manner (see also Fig. 14). The results indicate that the etherification of alcohols with long linear alkenes takes place at the external surface of the catalyst particles, and that alkenes were found mainly responsible for the coke formation and blockage of the external surface, which results in a loss of catalytic activity.

Outlook: Mesoporous Silica in Drug Delivery Applications

An intriguing perspective for mesoporous silica materials is their use as carriers in drug delivery applications, where they are employed to encapsulate var-

ious drugs or even RNA or DNA fragments and release them specifically at a target site. Especially the controlled release of cytotoxic antineoplastic drugs for cancer treatment in malignant cells could greatly enhance the efficacy of these drugs and simultaneously reduce the detrimental side effects of a chemotherapeutic treatment. In order to devise such systems, a great amount of control over the chemical properties of the porous silica materials as well as detailed knowledge about their behavior upon cell internalization and during the triggered release are of great importance. In the following, three examples are given that demonstrate how chemically modified mesoporous silica thin films or particles can be used in combination with single molecule microscopy studies to achieve this goal.

In a recent study, Lebold *et al.* demonstrated the feasibility of mesoporous silica thin films for the encapsulation and release of the anticancer drug doxorubicin, which is already widely used in clinical chemotherapy [90]. The authors investigated the influence of different templates (Pluronic P123, CTAB, and Brij56) and pore functionalizations on the drug dynamics inside the mesopores on a single molecule level. In thin films templated by the non-ionic triblock-copolymer Pluronic P123, a mobile sub-population of doxorubicin molecules could be observed at high drug loading rates, presumably due to the formation of doxorubicin dimers. However, the diffusional pathways of the drug inside the channel system were not very well structured. With the ionic template CTAB, the population of mobile molecules was about 10 %, and the trajectories indicating the diffusional movement of the drug showed a high degree of orientation. Interestingly, when the non-ionic block copolymer Brij56 was used, all molecules were immobile inside the film, presumably due to interactions of the guests with free hydroxyl groups at the channel surface, which were not shielded by an ionic counterpart (as in the case of the ionic template CTAB), and which were in close proximity to the guest molecules due to the smaller pore width (compared to silica thin films templated by Pluronic P123). This assumption is backed up by the fact that a mobile population could be recovered in the Brij56-templated samples by chemically modifying the silica pore walls with propyl groups. This must have led to a hydrophobization of the inner pore surface through a shielding of the hydroxyl groups, resulting in weaker interactions between the drug and the host matrix and hence a structured movement of the drug inside the porous host. Based on these findings, it was shown that the release kinetics of doxorubicin into the cell medium could be controlled by varying the template and the pore functionalization within the porous host, and that doxorubicin released from the film could be used to induce cell death in human cervical cancer (HeLa) cells. These findings suggest that for future applications, mesoporous silica structures could be used either in the form of film coatings for implants, *e. g.* for the delivery of immunosuppressive drugs to diminish rejection, or in the form of nanoparticles for drug-delivery applications.

Inspired by the previously described experiments, Lebold *et al.* further investigated ways to control the mobility of oligonucleotides (siRNA and dsDNA) within the nanochannels of mesoporous silica particles [47]. In order to do so, the authors focused on SBA-15 particles that were functionalized with aminopropyl, cyanoethyl and phenyl groups and compared them to unfunctionalized particles. They found that unfunctionalized and cyanoethyl-functionalized particles could not be loaded with siRNA, presumably due to the repulsive interaction of the negatively charged oligonucleotides with these functional groups. However, when adjusting the surface polarity of the silica pore walls by functionalization with aminopropyl groups, the unfavorable repulsive interactions were reduced, favorable interactions of the positively charged amino groups and the siRNA were created, and the particles could be loaded with siRNA. Moreover, the functionalized particles could also be loaded with dsDNA, ranging from 20 up to 90 base pairs in length. A detailed analysis of the movement of single oligonucleotide guest molecules revealed that the diffusion dynamics critically depend on the length of the oligonucleotides, and that long DNA sequences have a higher tendency to get immobilized at adsorption sites inside the porous framework. The stability of the oligonucleotides inside the porous silica host was proven for all nucleotides by Förster resonance energy transfer (FRET) experiments. The obtained information is of great importance for the design of mesoporous silica nanoparticles that can be used in gene therapy or gene silencing and for drug carriers featuring controlled retarded release of a drug over a prolonged period of time, generating a “depot effect”.

In order to tackle the challenge of controlled release at a target site, our groups investigated a vari-

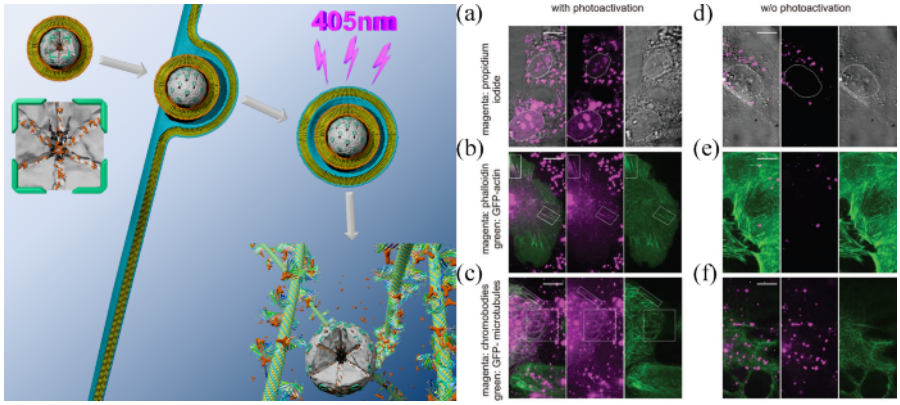

Fig. 15 (color online). Cascaded photoinduced release of various model drugs from multifunctional core-shell mesoporous silica particles sealed with a supported lipid bilayer. Left: Schematic representation of the process. Right: Confocal microscopy of living HuH7 cells exposed to the colloidal mesoporous silica nanoparticles carrying a photosensitizer and loaded with model drugs, sealed by a SLB. (a) Superposition of the transmitted light image of HuH7 cells with the propidium iodide (PI) fluorescence (left panel) and the PI fluorescence alone (center panel) and the transmitted light image (right panel). Propidium iodide stains the nucleus of the cell. (b) Alexa Fluor 647-labeled phalloidin fluorescence (shown in magenta) and stably actin-GFP (GFP: green fluorescent protein) expressing HuH7 cells (shown in green on the left panel), the phalloidin fluorescence channel alone (shown in magenta in the center panel) and the actin-GFP fluorescence channel (shown in green in the right panel). (c) Chromeo642-labeled chromobodies (magenta) released from the particles stain the microtubules of stably microtubule-GFP expressing HuH7 cells (green) (left panel). The chromobody channel is displayed in the center panel, the separated actin-GFP channel is shown in the right panel. (d–f). In case of the non-photoactivated samples, no labeled cell structure was observed. Scale bar: 10 μm. Reprinted with permission from ref. [96]. Copyright 2012 Wiley-VCH.

ety of different ways to enclose a drug inside porous silica particles and to release it as a result of specific external stimuli, including pH changes [91, 92], temperature changes [93], the presence of certain enzymes [94], and changes in the redox potential [95]. In a recent paper, Schlossbauer *et al.* demonstrated the cascaded photoinduced release of various model drugs from multifunctional core-shell mesoporous silica particles sealed with a supported lipid bilayer [96]. In this study, the model drugs propidium iodide, phalloidine, and small dye-labeled antibody fragments (chromobodies) were incorporated into multifunctional core-shell mesoporous silica particles [97, 98], carrying amino groups in the inner shell and thiol groups on the outer surface. This orthogonal, site-selective functionalization allowed for the specific covalent binding of a photosensitizer (Protoporphyrin IX) to the outer particle shell. Such photosensitizers are already used in photodynamic therapy to treat cancer. However, initial approaches of combining these photosensitizers with mesoporous silica as a drug carrier did not provide a covalent attachment, and could hence lead to uncontrolled leaching of the compounds from the particles, resulting in highly toxic effects on the cell. After covalent attachment of the photosensitizer and loading with drugs, the particles were sealed with a 1,2-dioleoyl-sn-glycero-3-phosphocholine (DOPC) supported lipid bilayer (SLB) membrane, constructed *via* a one-step solvent exchange route [99]. The formation of the SLB results in a tight encapsulation of the cargo molecules, preventing premature release of the model drugs from the particle. When the SLB-coated particles come into contact with cells, they are taken up *via* endocytosis and end up in an endosome inside the cell (see also Fig. 15). Upon illumination with light, the covalently bound photosensitizers produce highly reactive singlet oxygen that leads to the disintegration of the SLB around the particles [96]. Without the sealing, the model drugs can escape from the particles, but they are still trapped within the endosome. In a second step, the endosomal membrane is destroyed, which allows the model drugs to be released into the cytosol and reach their final destination. Strikingly, phototoxic effects (*e. g.* on microtubule motor proteins) were restricted to endosomes carrying nanoparticles, allowing for a "surgical" endosomal release without the global cell toxicity of common liquid-phase photosensitizers.

Summary

In this review article, we discussed how fluorescence microscopy can help us to broaden our understanding of some of the defining characteristics of porous silica compounds, such as their pore structure, interaction with guest molecules, and diffusion properties. We discussed the formation mechanism of porous silica thin films and gave a short overview of possible synthesis and functionalization techniques. We also gave an introduction into single molecule microscopy and elaborated on how it can help us to gain deeper insights into properties of porous silica host systems. Using some examples from the literature, we demonstrated how fluorescence microscopy helped elucidating important aspects of porous silica compounds and heterogeneous catalysis such as diffusion properties, reactivity, morphology, intergrowth, accessibility, and catalyst deactivation. We ended the article with a short outlook on the scope of porous silica compounds in drug delivery applications. We believe that fluorescence microscopy will continue to provide elegant and efficient ways to study the properties of this important class of materials in many future applications.

Acknowledgement

The authors wish to acknowledge all laboratory members that contributed to the original publications. Special thanks go to the long-term collaborator Professor K. Müllen, MPI for Polymer Research, Mainz. Financial support by the Nanosystems Initiative Munich (NIM), the Center for Integrated Protein Science Munich (CIPSM), the Center for NanoScience (CeNS) and the DFG-Sonderforschungsbereich (SFB) 749 as well as the DFG-Schwerpunkt 1313 is also gratefully acknowledged.

[1] M. J. Wirth, R. W. P. Fairbank, H. O. Fatunmbi, *Science* **1997**, *275*, 44 – 47.
[2] M. J. Wirth, D. J. Swinton, M. D. Ludes, *J. Phys. Chem. B* **2003**, *107*, 6258 – 6268.
[3] A. Corma, *Chem. Rev.* **1997**, *97*, 2373 – 2420.
[4] M. Jaroniec, *J. Am. Chem. Soc.* **2002**, *124*, 14506 – 14506.
[5] P. Pandey, S. Upadhyay, H. Pathak, *Sensors and Actuators B: Chemical* **1999**, *60*, 83 – 89.
[6] C.-Y. Lai, B. G. Trewyn, D. M. Jeftinija, K. Jeftinija, S. Xu, S. Jeftinija, V. S.-Y. Lin, *J. Am. Chem. Soc.* **2003**, *125*, 4451 – 4459.
[7] D. J. Bharali, I. Klejbor, E. K. Stachowiak, P. Dutta, I. Roy, N. Kaur, E. J. Bergey, P. N. Prasad, M. K. Stachowiak, *Proc. Natl. Acad. Sci. U. S. A.* **2005**, *102*, 11539 – 11544.
[8] V. Kukla, J. Kornatowski, D. Demuth, I. Girnus, H. Pfeifer, L. V. C. Rees, S. Schunk, K. K. Unger, J. Kärger, *Science* **1996**, *272*, 702 – 704.
[9] O. Terasaki, Z. Liu, T. Ohsuna, H. J. Shin, R. Ryoo, *Microsc. Microanal.* **2002**, *8*, 35 – 39.
[10] N. E. Benes, H. Jobic, H. Verweij, *Microp. Mesop. Mater.* **2001**, *43*, 147 – 152.
[11] R. M. Barrer, G. S. Perry, *J. Chem. Soc.* **1961**, 842 – 849.
[12] C. T. Kresge, M. E. Leonowicz, W. J. Roth, J. C. Vartuli, J. S. Beck, *Nature* **1992**, *359*, 710 – 712.
[13] G. J. d. A. A. Soler-Illia, C. Sanchez, B. Lebeau, J. Patarin, *Chem. Rev.* **2002**, *102*, 4093 – 4138.
[14] C. G. Goltner, M. Antonietti, *Adv. Mater.* **1997**, *9*, 431 – 436.
[15] D. Zhao, P. Yang, N. Melosh, J. Feng, B. F. Chmelka, G. D. Stucky, *Adv. Mater.* **1998**, *10*, 1380 – 1385.
[16] I. A. Aksay, M. Trau, S. Manne, I. Honma, N. Yao, L. Zhou, P. Fenter, P. M. Eisenberger, S. M. Gruner, *Science* **1996**, *273*, 892 – 898.
[17] M. Ogawa, *Chem. Commun.* **1996**, *0*, 1149 – 1150.
[18] H. Yang, A. Kuperman, N. Coombs, S. Mamiche-Afara, G. A. Ozin, *Nature* **1996**, *379*, 703 – 705.
[19] C. J. Brinker, Y. Lu, A. Sellinger, H. Fan, *Adv. Mater.* **1999**, *11*, 579 – 585.
[20] Y. Lu, R. Ganguli, C. A. Drewien, M. T. Anderson, C. J. Brinker, W. Gong, Y. Guo, H. Soyez, B. Dunn, M. H. Huang, J. I. Zink, *Nature* **1997**, *389*, 364 – 368.
[21] M. Ogawa, *J. Am. Chem. Soc.* **1994**, *116*, 7941 – 7942.
[22] D. A. Doshi, A. Gibaud, V. Goletto, M. Lu, H. Gerung, B. Ocko, S. M. Han, C. J. Brinker, *J. Am. Chem. Soc.* **2003**, *125*, 11646 – 11655.
[23] D. Grosso, F. Babonneau, P.-A. Albouy, H. Amenitsch, A. R. Balkenende, A. Brunet-Bruneau, J. Rivory, *Chem. Mater.* **2002**, *14*, 931 – 939.
[24] B. Smarsly, A. Gibaud, W. Ruland, D. Sturmayr, C. J. Brinker, *Langmuir* **2005**, *21*, 3858 – 3866.
[25] D. Grosso, A. R. Balkenende, P. A. Albouy, A. Ayral, H. Amenitsch, F. Babonneau, *Chem. Mater.* **2001**, *13*, 1848 – 1856.
[26] J. S. Beck, J. C. Vartuli, W. J. Roth, M. E. Leonowicz, C. T. Kresge, K. D. Schmitt, C. T. W. Chu, D. H. Olson, E. W. Sheppard, *J. Am. Chem. Soc.* **1992**, *114*, 10834 – 10843.

[27] G. S. Attard, J. C. Glyde, C. G. Goltner, *Nature* **1995**, *378*, 366 – 368.
[28] Y. Wan, Zhao, *Chem. Rev.* **2007**, *107*, 2821 – 2860.
[29] C. Jung, P. Schwaderer, M. Dethlefsen, R. Köhn, J. Michaelis, C. Bräuchle, *Nature Nanotech.* **2011**, *6*, 87 – 92.
[30] C. Sanchez, C. Boissière, D. Grosso, C. Laberty, L. Nicole, *Chem. Mater.* **2008**, *20*, 682 – 737.
[31] R. Fan, S. Huh, R. Yan, J. Arnold, P. Yang, *Nat. Mater.* **2008**, *7*, 303 – 307.
[32] H. Luo, D. Wang, J. He, Y. Lu, *J. Phys. Chem. B* **2005**, *109*, 1919 – 1922.
[33] P. Yang, G. Wirnsberger, H. C. Huang, S. R. Cordero, M. D. McGehee, B. Scott, T. Deng, G. M. Whitesides, B. F. Chmelka, S. K. Buratto, G. D. Stucky, *Science* **2000**, *287*, 465 – 467.
[34] C.-W. Wu, T. Ohsuna, T. Edura, K. Kuroda, *Angew. Chem. Int. Ed.* **2007**, *46*, 5364 – 5368.
[35] H. Daiguji, N. Tatsumi, S. Kataoka, A. Endo, *Langmuir* **2009**, *25*, 11221 – 11224.
[36] E. Kim, Y. Xia, G. M. Whitesides, *Nature* **1995**, *376*, 581 – 584.
[37] M. Trau, N. Yao, E. Kim, Y. Xia, G. M. Whitesides, I. A. Aksay, *Nature* **1997**, *390*, 674 – 676.
[38] S. H. Tolbert, A. Firouzi, G. D. Stucky, B. F. Chmelka, *Science* **1997**, *278*, 264 – 268.
[39] H. Miyata, K. Kuroda, *J. Am. Chem. Soc.* **1999**, *121*, 7618 – 7624.
[40] H. Miyata, Y. Kawashima, M. Itoh, M. Watanabe, *Chem. Mater.* **2005**, *17*, 5323 – 5327.
[41] D. Zhao, J. Feng, Q. Huo, N. Melosh, G. H. Fredrickson, B. F. Chmelka, G. D. Stucky, *Science* **1998**, *279*, 548 – 552.
[42] S. P. Naik, S. Yamakita, M. Ogura, T. Okubo, *Microp. Mesop. Mater.* **2004**, *75*, 51 – 59.
[43] B. Ruehle, M. Davies, T. Lebold, C. Bräuchle, T. Bein, *ACS Nano* **2012**, *6*, 1948 – 1960.
[44] H. Miyata, K. Kuroda, *Chem. Mater.* **1999**, *12*, 49 – 54.
[45] H. Miyata, T. Noma, M. Watanabe, K. Kuroda, *Chem. Mater.* **2002**, *14*, 766 – 772.
[46] T. Lebold, L. A. Mühlstein, J. Blechinger, M. Riederer, H. Amenitsch, R. Köhn, K. Peneva, K. Müllen, J. Michaelis, C. Bräuchle, T. Bein, *Chem. Eur. J.* **2009**, *15*, 1661 – 1672.
[47] T. Lebold, A. Schlossbauer, K. Schneider, L. Schermelleh, H. Leonhardt, T. Bein, C. Bräuchle, *Adv. Funct. Mater.* **2012**, *22*, 106 – 112.
[48] F. Feil, V. Cauda, T. Bein, C. Bräuchle, *Nano Lett.* **2012**, *12*, 1354 – 1361.
[49] S. L. Burkett, S. D. Sims, S. Mann, *Chem. Commun.* **1996**, *0*, 1367 – 1368.
[50] D. J. Macquarrie, *Chem. Commun.* **1996**, *0*, 1961 – 1962.
[51] M. H. Lim, A. Stein, *Chem. Mater.* **1999**, *11*, 3285 – 3295.
[52] A. Zürner, J. Kirstein, M. Döblinger, C. Bräuchle, T. Bein, *Nature* **2007**, *450*, 705 – 708.
[53] J. Kirstein, B. Platschek, C. Jung, R. Brown, T. Bein, C. Bräuchle, *Nat. Mater.* **2007**, *6*, 303 – 310.
[54] F. Feil, C. Jung, J. Kirstein, J. Michaelis, C. Li, F. Nolde, K. Müllen, C. Bräuchle, *Microp. Mesop. Mater.* **2009**, *125*, 70 – 78.
[55] W. E. Moerner, L. Kador, *Phys. Rev. Lett.* **1989**, *62*, 2535 – 2538.
[56] M. Orrit, J. Bernard, *Phys. Rev. Lett.* **1990**, *65*, 2716 – 2719.
[57] 1st Nobel Conference of "Single Molecules in Physics, Chemistry and Biology", *Single Molecule Spectroscopy: Nobel Conference Lectures*, Springer, Berlin Heidelberg **2001**.
[58] 2nd Nobel Conference of "Single Molecules in Physics, Chemistry and Biology", *Single Molecule Spectroscopy in Chemistry, Physics and Biology: Nobel Symposium*, Vol. 96, Springer, Berlin Heidelberg **2010**.
[59] S. Weiss, *Science* **1999**, *283*, 1676 – 1683.
[60] P. Tamarat, A. Maali, B. Lounis, M. Orrit, *J. Phys. Chem. A* **1999**, *104*, 1 – 16.
[61] W. E. Moerner, *J. Phys. Chem. B* **2002**, *106*, 910 – 927.
[62] A. Yamaguchi, F. Uejo, T. Yoda, T. Uchida, Y. Tanamura, T. Yamashita, N. Teramae, *Nat. Mater.* **2004**, *3*, 337 – 341.
[63] B. Platschek, N. Petkov, T. Bein, *Angew. Chem. Int. Ed.* **2006**, *45*, 1134 – 1138.
[64] D. A. Higgins, M. M. Collinson, G. Saroja, A. M. Bardo, *Chem. Mater.* **2002**, *14*, 3734 – 3744.
[65] S. A. Martin-Brown, Y. Fu, G. Saroja, M. M. Collinson, D. A. Higgins, *Anal. Chem.* **2004**, *77*, 486 – 494.
[66] E. Mei, A. M. Bardo, M. M. Collinson, D. A. Higgins, *J. Phys. Chem. B* **2000**, *104*, 9973 – 9980.
[67] C. Cui, A. Kirkeminde, B. Kannan, M. M. Collinson, D. A. Higgins, *J. Phys. Chem. C* **2010**, *115*, 728 – 735.
[68] Y. Fu, F. Ye, W. G. Sanders, M. M. Collinson, D. A. Higgins, *J. Phys. Chem. B* **2006**, *110*, 9164 – 9170.
[69] F. Ye, D. A. Higgins, M. M. Collinson, *J. Phys. Chem. C* **2007**, *111*, 6772 – 6780.
[70] C. Hellriegel, J. Kirstein, C. Bräuchle, V. Latour, T. Pigot, R. Olivier, S. Lacombe, R. Brown, V. Guieu, C. Payrastre, A. Izquierdo, P. Mocho, *J. Phys. Chem. B* **2004**, *108*, 14699 – 14709.
[71] C. Hellriegel, J. Kirstein, C. Bräuchle, *New J. Phys.* **2005**, *7*, 23.
[72] C. Jung, C. Hellriegel, B. Platschek, D. Wöhrle, T. Bein, J. Michaelis, C. Bräuchle, *J. Am. Chem. Soc.* **2007**, *129*, 5570 – 5579.

[73] C. Jung, J. Kirstein, B. Platschek, T. Bein, M. Budde, I. Frank, K. Müllen, J. Michaelis, C. Bräuchle, *J. Am. Chem. Soc.* **2008**, *130*, 1638 – 1648.
[74] G. De Cremer, E. Bartholomeeusen, P. P. Pescarmona, K. Lin, D. E. D. Vos, J. Hofkens, M. B. Roeffaers, B. F. Sels, *Catal. Today* **2010**, *157*, 236 – 242.
[75] L. Karwacki, E. Stavitski, M. H. F. Kox, J. Kornatowski, B. M. Weckhuysen, *Angew. Chem. Int. Ed.* **2007**, *46*, 7228 – 7231.
[76] L. Karwacki, M. H. F. Kox, D. A. Matthijs de Winter, M. R. Drury, J. D. Meeldijk, E. Stavitski, W. Schmidt, M. Mertens, P. Cubillas, N. John, A. Chan, N. Kahn, S. R. Bare, M. Anderson, J. Kornatowski, B. M. Weckhuysen, *Nat. Mater.* **2009**, *8*, 959 – 965.
[77] L. Sommer, S. Svelle, K. P. Lillerud, M. Stöcker, B. M. Weckhuysen, U. Olsbye, *Langmuir* **2010**, *26*, 16510 – 16516.
[78] M. B. J. Roeffaers, R. Ameloot, A.-J. Bons, W. Mortier, G. De Cremer, R. de Kloe, J. Hofkens, D. E. De Vos, B. F. Sels, *J. Am. Chem. Soc.* **2008**, *130*, 13516 – 13517.
[79] M. B. J. Roeffaers, G. De Cremer, J. Libeert, R. Ameloot, P. Dedecker, A.-J. Bons, M. Bueckins, J. A. Martens, B. F. Sels, D. E. De Vos, J. Hofkens, *Angew. Chem. Int. Ed.* **2009**, *48*, 9285 – 9289.
[80] M. H. F. Kox, A. Mijovilovich, J. J. H. B. Sättler, E. Stavitski, B. M. Weckhuysen, *ChemCatChem* **2010**, *2*, 564 – 571.
[81] Y.-M. Chung, D. Mores, B. M. Weckhuysen, *Appl. Cat. A* **2011**, *404*, 12 – 20.
[82] I. L. C. Buurmans, J. Ruiz-Martinez, W. V. Knowles, D. van der Beek, J. A. Bergwerff, E. T. C. Vogt, B. M. Weckhuysen, *Nat. Chem.* **2011**, *3*, 862 – 867.
[83] M. A. Karreman, I. L. C. Buurmans, J. W. Geus, A. V. Agronskaia, J. Ruiz-Marinez, H. C. Gerritsen, B. M. Weckhuysen, *Angew. Chem. Int. Ed.* **2012**, *51*, 1428 – 1431.
[84] E. Stavitski, M. H. F. Kox, B. M. Weckhuysen, *Chem. Eur. J.* **2007**, *13*, 7057 – 7065.
[85] M. H. F. Kox, E. Stavitski, J. C. Groen, J. Pérez-Ramirez, F. Kapteijn, B. M. Weckhuysen, *Chem. Eur. J.* **2008**, *14*, 1718 – 1725.
[86] K. F. Domke, T. A. Riemer, G. Rago, A. N. Parvulescu, P. C. A. Bruijnincx, A. Enejder, B. M. Weckhuysen, M. Bonn, *J. Am. Chem. Soc.* **2012**, *134*, 1124 – 1129.
[87] J. Ruiz-Marinez, I. L. Buurmans, W. V. Knowles, D. van der Beek, J. A. Bergwerff, E. T. Vogt, B. M. Weckhuysen, *Appl. Cat. A* **2012**, *419 – 420*, 84 – 94.
[88] D. Mores, E. Stavitski, S. P. Verkleij, A. Lombard, A. Cabiac, L. Rouleau, J. Patarin, A. Simon-Masseron, B. M. Weckhuysen, *Phys. Chem. Chem. Phys.* **2011**, *13*, 15985 – 15994.
[89] A. N. Parvulescu, D. Mores, E. Stavitski, C. M. Teodorescu, P. C. A. Bruijnincx, R. J. M. K. Gebbink, B. M. Weckhuysen, *J. Am. Chem. Soc.* **2010**, *132*, 10429 – 10439.
[90] T. Lebold, C. Jung, J. Michaelis, C. Bräuchle, *Nano Lett.* **2009**, *9*, 2877 – 2883.
[91] V. Cauda, C. Argyo, A. Schlossbauer, T. Bein, *J. Mater. Chem.* **2010**, *20*, 4305 – 4311.
[92] A. Schlossbauer, C. Dohmen, D. Schaffert, E. Wagner, T. Bein, *Angew. Chem. Int. Ed.* **2011**, *50*, 6828 – 6830.
[93] A. Schlossbauer, S. Warncke, P. M. E. Gramlich, J. Kecht, A. Manetto, T. Carell, T. Bein, *Angew. Chem. Int. Ed.* **2010**, *49*, 4734 – 4737.
[94] A. Schlossbauer, J. Kecht, T. Bein, *Angew. Chem. Int. Ed.* **2009**, *48*, 3092 – 3095.
[95] A. M. Sauer, A. Schlossbauer, N. Ruthardt, V. Cauda, T. Bein, C. Bräuchle, *Nano Lett.* **2010**, *10*, 3684 – 3691.
[96] A. Schlossbauer, A. M. Sauer, V. Cauda, A. Schmidt, H. Engelke, U. Rothbauer, K. Zolghadr, H. Leonhardt, C. Bräuchle, T. Bein, *Adv. Healthcare Mater.* **2012**, *1*, 316 – 320.
[97] J. Kecht, A. Schlossbauer, T. Bein, *Chem. Mater.* **2008**, *20*, 7207 – 7214.
[98] V. Cauda, A. Schlossbauer, J. Kecht, A. Zürner, T. Bein, *J. Am. Chem. Soc.* **2009**, *131*, 11361 – 11370.
[99] V. Cauda, H. Engelke, A. Sauer, D. Arcizet, C. Bräuchle, J. Rädler, T. Bein, *Nano Lett.* **2010**, *10*, 2484 – 2492.